Modelling and characterisation of ultrasonic joints for Li-ion batteries to evaluate the impact on electrical resistance and temperature raise

Abhishek Das[*, 1], T.R Ashwin[1], Anup Barai[1]

[1] *WMG, The University of Warwick, Coventry, CV4 8GJ, United Kingdom*
[*]Corresponding Author: Abhishek Das, A.Das.1@warwick.ac.uk

Abstract

In automotive and stationary Li-ion battery packs, a large number of individual cells, typically hundreds to thousands of cells, are electrically connected to achieve pack specification. These large number of interconnections are mainly achieved by welding cell tab to bus-bar using a welding technique of choice. Ultrasonic metal welding (UMW) is one of the common joining technique employed to join pouch cell's tabs to bus-bar. Although commonly employed, there is little research currently exist in literature reporting the joint characteristics in terms of electrical resistance and temperature raise due to charge-discharge current. Li-ion batteries reaching sub-milliohm internal resistance, risks the temperature raise at the joint could be even higher than the cell itself which raise a serious safety concern and they are to be addressed. This research investigates the electrical and thermal characteristics of ultrasonic joints of 0.3 mm aluminium/nickel coated copper tabs to 1.0 mm copper bus-bar. This article reports the dynamic behaviour of electrical resistance and corresponding temperature increase as a result of current flow. To capture the electrical and thermal behaviour of the joint, a numerical model has been developed and validated with experimental results, which can be employed to analyse battery pack performance.

Keywords: Ultrasonic metal welding; electric vehicle battery assembly; contract resistance; temperature raise, conjugate heat transfer

1. Introduction

In recent years, different carbon emission legislation has been set-out by different national and international legislative authorities to reduce emission of greenhouse gases [1, 2]; in UK, one such legislation is 'The Climate Change Act', which sets the target of reducing the greenhouse gas emissions by 80 % of 1990 figure within 2050 [3]. Such legislations are the key driver for the automotive industry to develop and promote hybrid (HEV) and fully electric vehicles (EV).

With recent advancement of Lithium-ion (Li-ion) battery technology, it is currently the technology of choice for EVs and HEVs, also progressively finding its way to provide Grid service as large scale energy storage system for grid [4, 5].

Typically, large Li-ion battery packs, such used in automotive industry consists of hundreds to thousands of battery cells, which are electrically connected and structurally held within a module. These large number of cells within the pack are arranged in several modules, where they are connected to bus-bars. Number of cells within a module and number of modules within a pack depend on required maximum energy storage capability, amperage and voltage, to deliver the necessary power and driving range. Often, these battery packs are exposed to harsh operating conditions e.g. high power demand, high and low temperature, vibration, all such conditions led to the requirement of electrically and thermally efficient and durable cell tab to bus-bar interconnect joints.

In existing commercial battery packs, cell tab to bus-bar joints are carried by numerous joining/welding processes including ultrasonic welding, resistance spot welding, pulsed arc welding or laser welding [6-8]. For pouch cell based tab-to-busbar connection, ultrasonic metal welding is the most common joining method used by battery manufacturers due to several advantages, such as, dissimilar metals joining, varying thicknesses of different stack-up conditions, good joining methods for electrically conductive and highly reflective tab or busbar materials, and multiple stack-up joining. In spite of several advantages of ultrasonic metal welding for joining tab-to-busbar, there are few issues to be addressed, one such is the electrical resistance at the joint, which led to temperature raise during charge-discharge. With the trajectory of lithium-ion battery cells heading to sub-milliohm internal resistance there is a real chance that there will be high amount of resistive heat generation at the joint, which can lead to high temperature raise, even higher than the cell itself which raise a serious safety concern.

In general, ultrasonic metal welding has been widely used for the production of cells, pouch cell based modules, and subsequently battery packs. Tab-to-busbar joints are the elementary connections which are to be made in large number, up to thousands, to build an automotive battery packs. Evaluation of these tab to bus-bar joints is essential to determine joint electrical and thermal behaviour. Although of high importance, ultrasonic metal welding techniques received little research attention compared to the development and modelling of the Li-ion cell. For example, comprehensive research has been undertaken focusing on Li-ion battery chemistry, power capacity improvements, material development, modelling and simulation,

performance enhancements or battery testing and characterisation, and safety [9-11]. However, the joining aspects of the Li-ion cells are mainly limited to metallurgical and mechanical characterisation of joining process [12-14]. There are a few literature available focusing on the comprehensive performance, characterisation and modelling of electrical resistance and thermal behaviours of the tab to bus-bar joints. To measure the electrical contact resistance, Brand, et al. [7] developed measuring and calculation method using cylindrical cells to external conductor (i.e. cylindrical cell terminal to tab connection) and compared three different welding techniques (i.e. resistance spot, ultrasonic and laser beam welding) to evaluate contact resistance occurred as a result of the joint. Furthermore, they obtained minimum electrical contact resistance of 0.169 mΩ for CuZn37 specimens to negative terminal of 26650 lithium-ion cell made of nickel-plated steel. To understand the ultrasonic joining mechanism, Cai, et al. [15] demonstrated the heat generation as a result of friction between the mating parts during the welding process using finite element analysis. Similar to them, Li, et al. [16] conducted a series of experiments to investigate the dynamic heat generation during the ultrasonic metal welding process. However, detailed investigations are required for the ultrasonic metal welded joints when they are in use for battery pack applications. To date, a little research have been published to understand the electrical and thermal behaviour of ultrasonic tab to bus-bar welds. This article aims to characterise and model contact resistance and thermal behaviour of the joint when charge-discharge current is passed. Readers interested in relationship between mechanical strength and contact resistance, and metallurgical characterisation are redirected to the Ni and Ye [17], Shakil, et al. [14] and Brand, et al. [7].

The remainder of this paper is arranges as follows: Section 2 provides an overview of ultrasonic welding mechanism, joining principle and experimental test set-up; Section 3 lays out the experimental plan, electrical and temperature measurement details; Section 4 describes the modelling methodology to characterise electrical and thermal behaviour of ultrasonic metal welded joints; the results and discussions are made in Section 5; and conclusions are drawn in Section 6.

2. Overview of ultrasonic welding mechanism

Making the required battery tab to bus-bar joint is not trivial as it poses several challenges including joining of highly conductive and reflective materials, such as aluminium and copper; joining of dissimilar multiple, thin, stack-up materials having different melting temperatures; protecting the cell from potential damage (i.e. thermal, mechanical or vibrational) during

joining; and providing durable joint which satisfies the mechanical strength at par with the electrical and thermal requirements. Ultrasonic metal welding (UMW) is a suitable joining technique for joining dissimilar thin to thick materials [8, 14] and capable of joining highly conductive/reflective materials. Furthermore, the ultrasonic welding does not depend on the absolute melting temperature of the substrate materials as it is a solid state welding process where electrical energy is converted into high frequency mechanical vibration to generate heat between joining surfaces [18, 19] and ultrasonic energy is used to produce oscillating shear forces to create solid-state bonds between two sheets clamped under pressure [20]. However, this joining technique requires two sided access; on one side the anvil to supports the parts to be joined where the part may have varying thicknesses, on the other side a sonotrode passes ultrasonic energy to the assembly as illustrated in Fig. 1. The required welding energy depends on the thickness, hardness and density of the materials which are to be vibrated by the sonotrode. However, some difficulties may be observed when joining hard materials such as steel and additionally, this joining technique is not suitable for thick and hard materials.

Often ultrasonic metal welding is used for tab to bus-bar joints of pouch cells. Ultrasonic metal welding is considered to be the best joining process when welding varying stack-ups and has good weldability for dissimilar materials that typically produce brittle alloys at the weld area [21, 22]. Due to these favourable conditions, ultrasonic metal welding is considered a superior process for pouch cell tab to bus-bar joining [23, 24]. However, it was reported that excessive ultrasonic vibration can damage the inside electrochemical arrangement of the pouch cell and sufficient clamping mechanism is required to prevent propagation of vibration into the pouch cell [25]. UMW has been used to join the battery packs for various electric and plug-in hybrid vehicles, including the Nissan LEAF, General Motors's (GM) Chevy Volt, Spark and Bolt [16, 26].

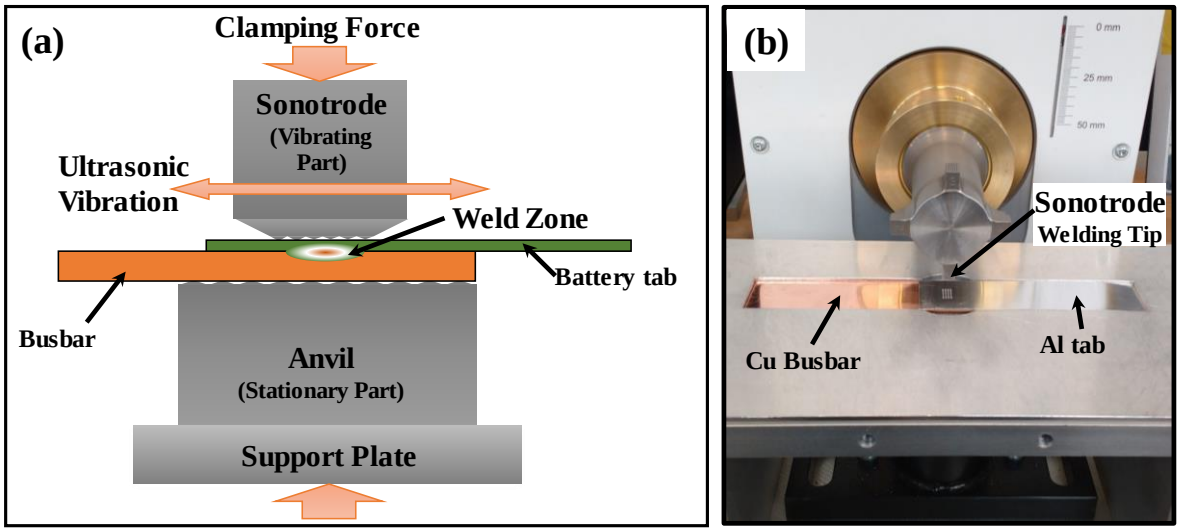

Fig. 1 Ultrasonic metal welding (a) illustration of welding principle, and (b) tab-to-busbar joining set-up.

3. Experimental details

Detailed experimental plan, test set-ups and materials used for experimentation are described in this section.

3.1. Investigated materials and sample preparation

The primary objective of this study is to evaluate the electrical resistance and temperature raise at tab-to-busbar interconnect during charging and discharging of battery cells. Therefore, the tab and busbar materials are chosen to represent a battery tab-to-busbar production application. The most commonly used tab and busbar materials, especially for pouch cell tab-to-busbar connection application, are either aluminium (Al) tabs or nickel-coated copper (Cu[Ni]) tabs (electrolytically nickel-plated copper strips of approximately 2 µm Ni coating is mainly used for corrosion resistance) and aluminium (Al) busbar or copper (Cu) busbar. Commercially available and production representative tab and busbar materials used for this study are listed in Table 1. The 0.3 mm thick tabs are the most commonly used for high power high energy cells. In general, the busbar thickness and choice of material are based on maximum current carrying capacity requirements, availability of busbar cooling, weight, and cost. As the objectives of this study are to model and determine the electrical and thermal behaviours of the joint, this study uses 1 mm copper bus-bar to weld with two different tab materials, i.e. aluminium (Al) and nickel-coated copper (Cu[Ni]) as a case-in-point. The test samples were prepared in lap configuration using ultrasonic metal welding. Schematic of tab-to-busbar

interconnect test specimen is illustrated in **Fig. 2**. Using UMW, the test specimens were prepared where the busbar was kept as lower part and tab material was as upper part.

Table 1 Tab and busbar materials used for experimental investigations

Material Details			
Type	**Material**	**Specification**	**Nominal Thickness [mm]**
Tabs	Aluminium (Al)	AW1050A-H18; BS EN546	0.3
	Nickel-coated Copper (Cu[Ni])	CW004A-H040; BS EN1652 (C101Sl BS2870)	0.3
Busbar	Copper (Cu)	CW004A-H065; BS EN1652 (C101HH; BS 2870)	1.0

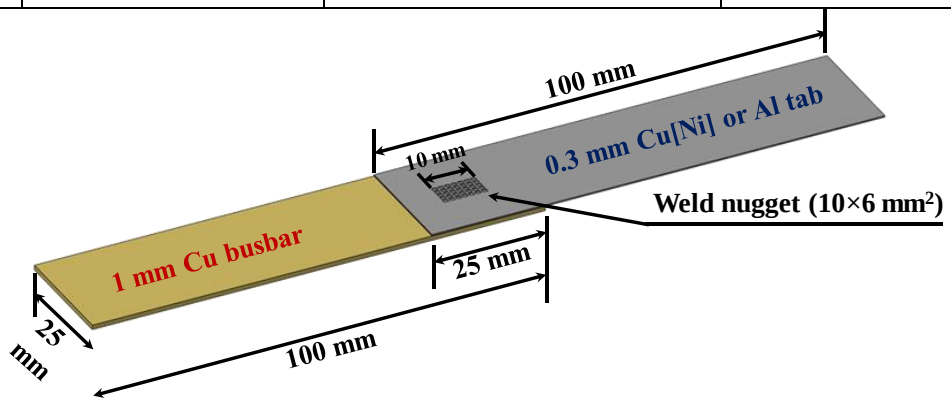

(a)

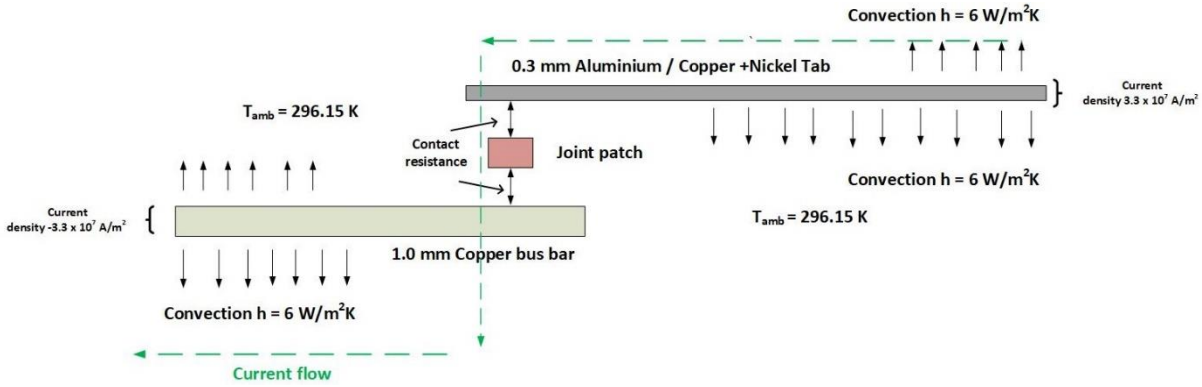

(b)

Fig. 2 (a) A pictorial example of ultrasonic welding to produce tab to bus-bar interconnect, (b) showing the bus-bar, tab and joint as additional block with thermal modelling details.

3.2. Process parameters for ultrasonic metal welding

Ultrasonic metal welding was conducted using welding energy as the main controlling parameter where ultrasonic operation remained active until the target energy was reached.

When welding in constant welding energy mode, the welding time varies slightly and depends primarily on the welding pressure and amplitude. The sonotrode used for this application can create ultrasonic welds of 10×6 mm^2 area and ultrasonic frequency was 20 kHz. The amplitude for the ultrasonic vibration was kept constant at 80% of the coded value (100% peak to peak amplitude corresponds to 60 μm) and the working pressure held at 2.5 bar. After carrying out the welding, the same 2.5 bar pressure was applied as holding pressure for 0.3 seconds. The trigger mode time was set at 0.2 seconds which allowed conversion of the traversing pressure to welding pressure. In order to determine the ideal process conditions for each stack-up combination, initial pilot runs were conducted to identify the process window and suitable joining parameters. Based on the pilot experimental results, joining parameters were selected for producing the welds. When conducting the joining, copper bus-bar was used as lower part and Ni-coated copper or aluminium tabs were used as upper part because ultrasonic welding was preferred as thin to thick section joining. For ultrasonic welding of 0.3 mm Al and Cu[Ni] tabs to 1 mm Cu bus-bar, ultrasonic energies of 70 Ws and 600 Ws were used respectively based on the pilot experimental results to produce satisfactory welds.

3.3. Test set-up for electrical and thermal characterisation

The main objective of this paper is to characterise the electrical resistance coupled with temperature raise at the tab to bus-bar joints using production representative tab and busbar materials. The test set-up is shown in Fig. 3. The welded busbar and tab was connected with a power supply using a brass block, a separate voltage sensor was connected at same point. To measure the electrical resistance, current was passed through the welded busbar and voltage was measured. Resistance was calculated from the induced voltage due to application of the current. When current is applied resistive heat loss ($I^2 R_{weld}$) at the point of weld heats-up the welded location. To measure the temperature raise a thermal camera was used, it was placed on top of the welded location (Fig. 3). Heat generation and thus the temperature raise is directly linked to the current amplitude used, therefore, in this experiment current values of 150, 200 and 250 amp were employed for 60 sec each. After each current were employed for 60 sec, the welded location were allowed to cool down to the room temperature (~23°C) before next current value was applied. The resistance is not expected to change as a function of the current amplitude, however, the heat generation and the heat dissipation to the environment will be, which will change the resistance. The results from different current amplitude results will enable the modelling of the heat dissipation.

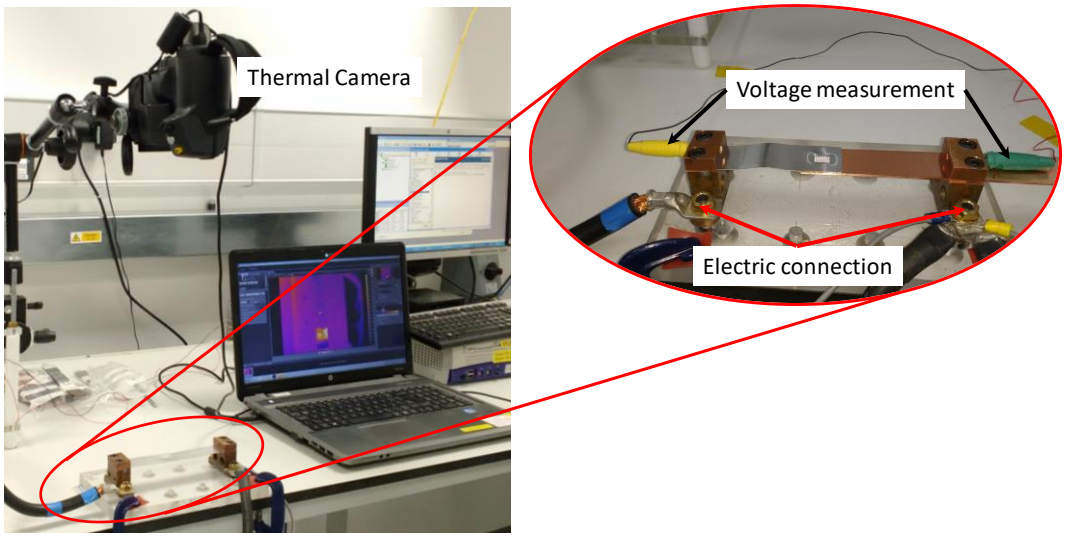

Fig. 3 Test set-up for electrical and thermal characterisation of tab to bus-bar joints.

4. Electrical and thermal modelling methodology

Numerical modelling of the weld geometry is completed using the finite volume based Computational Fluid Dynamics (CFD) solver ANSYS FLUENT. The geometry is divided into three regions namely copper bus-bar, aluminium/nickel-coated tab and the patch or weld region as shown in Fig. 2(b). The metal surfaces linked to these regions and exposed to ambient air flow are identified and labelled separately in the software. This will be helpful for imposing different boundary conditions and convective heat transfer coefficient at the metal surface. Structured hexagonal mesh is generated using ICEM-CFD solver which allows the use of higher order numerical schemes for calculation. The quality of the mesh is ensured by keeping the determinant above 0.9 and the warpage below 0.45. Correct boundary conditions can be imposed in ICEM-CFD software before exporting the mesh to solver Fluent. The boundary conditions can also be modified in FLUENT software, if necessary. All the overlapping regions are declared interior which ensures the flux continuity throughout the domain.

Correct material properties were assigned to three regions from FLUENT database. A grid sensitivity analysis is conducted for the consistency of results and the optimum number of nodal points were found to be 8000. The results of this sensitivity studies are not reported in this work for brevity. However, due care is given to use at least three control volumes in the thinnest regions. Therefore, to resolve the patch between two metal plates, and to capture the temperature distribution without any visual discontinuity, the geometry is divided into 13000 nodal points. A steady state formulation is adapted, and the simulation requires 20000 iterations to reach steady state. The algorithm used in this calculation is SIMPLE (Semi-Implicit Method

for Pressure Linked Equations). However, the flow equations are disabled due to solid domain (or assumed infinite viscosity) which effectively solve the energy equation in the following form:

$$\frac{\partial}{\partial t}(\rho E) = \nabla.\left(\lambda\, \nabla \mathrm{T} - \sum_j H_j J_j + \tau\,.\vec{v}\right) + S \qquad (1)$$

Where $E = H - \frac{P}{\rho} + \frac{v^2}{2}$ is the internal energy, λ the thermal conductivity, J is the diffusion flux of species, H is the enthalpy of the species, τ is the shear stress due to turbulence and S represents the source terms. In the absence of velocity and turbulent shear stress for a single species, the above energy equation reduces to a conjugate form:

$$\frac{\partial}{\partial t}\left(\rho C_p\right) = \nabla.\left(\lambda\, \nabla \mathrm{T}\right) + hA_s(T_\infty - T) + I^2 R_c \qquad (2)$$

Where $I^2 R_c$ is the volumetric heat generation due to ohmic resistance. Where ρ is the density of the solid domain, C_p specific heat, h convective heat transfer coefficient over the surface, R_c is the electrical resistance of the solid. Joule heating term $I^2 R_c$ has contributions from the contact resistance of weld region as well as the electrical resistance of the metal.

The gradient at control volume faces are computed in fluent using least square cell-based construction which assumes a linear variation of the solution between two nodal points. The flux at the control volume face is calculated from the centroid of control volume 1 and 2 along vector δr can be expressed as:

$$\nabla\varphi.\,\Delta r = \varphi_{cell2} - \varphi_{cell1} \qquad (3)$$

This third-order accurate MUSCL (Monotone Upstream Centred Schemes for Conservation Laws) is used for discretising conduction term. The MUSCL scheme is applicable to any mesh types structured or unstructured and has the potential to improve spatial accuracy by reducing numerical diffusion.

The heat energy generated due to ohmic heating is conducted to the surface of metal. Transfer of energy from surface of metal to the layer of air adjacent (broadly referred to as the Boundary later) is also due to heat conduction. This process is governed by the Fourier heat conduction equation. Convection happens due to the molecular movement from the layer of air adjacent to the metal surface to the bulk, which is at ambient temperature. This is under the assumption that there is no accumulation of energy during the chain of energy cascading. The above process is described by the flux continuity is applied at the metal surface as follows:

$$-\lambda \frac{\partial T}{\partial x}\Big|_{surface} = hA_s(T_\infty - T) \quad (4)$$

As explained earlier, SIMPLE algorithm frame work is used for solving even though the convective terms are completely absent. More details about the algorithm and solution method is presented in Ashwin, et al. [27].

Initial and boundary conditions

A steady state pressure based solver setting is selected for simulation. The energy equation is switched on and the flow equations are switched off. The model is initialised with temperature of 296.15K over the entire domain. A DC current of 250A is applied at the ends of the geometry which generates joules heating. There are two methods for inputting this boundary condition; by specifying the potential difference or by specifying the current flux. A current flux of 3.3×10^7 A/cm^2 is applied at Aluminium tab clamp for 250A condition and flux of same negative magnitude is applied at the Copper bus bar clamp as shown in Figure 2a. As current flows, the metallic current path will get heat up. In contrast, higher convective heat transfer coefficient at surface of metal can lower surface temperature. Therefore, the temperature profile over metal surface is a strong function of applied current, contact resistance of the weld joint and the convective heat transfer coefficient on the metal surface. For parameterising the model, measured contact resistance will be used and the surface heat transfer coefficient will be adjusted. The initial and boundary conditions for the model is summarised in Table 2.

Table 2. Property of material with initial and boundary condition

Surface	**Material**	**Heat transfer coefficient W/m2K**	**Current flux A/m2**	**Initial temperature (K)**	**Dimensions**	
					Length (m)	**Area (m2)**
Aluminium tab	Aluminium	6	0	296.15	0.1	----
Copper bus bar	Copper	6	0	296.15	0.1	----
Joint patch	Copper (Assumed)	6	0	296.15	0.025	----
Aluminium end clamp	Aluminium	6	3.3×10^7	296.15	------	7.5×10^{-6}
Copper end clamp	Copper	6	-3.3×10^7	296.15	----	2.5×10^{-5}
Material property						
	Density kg/m3	**Specific heat J/kg K**	**Thermal conductivity W/m-K**	**Electrical conductivity simens/m**		
Aluminium	2719	871	202.4	3.54×10^7		
Copper	8978	381	387.6	5.8×10^7		

5. Results and discussion

This section reports the result obtained from the electrical resistance tests and temperature raise as a result of current passing through the joint. Furthermore, it compares the joint temperature result from modelling and physical test data.

5.1. Joint resistance behaviour

The electrical resistance was determined from the measured induced voltage using the test set-up as described in Section 3.3. In

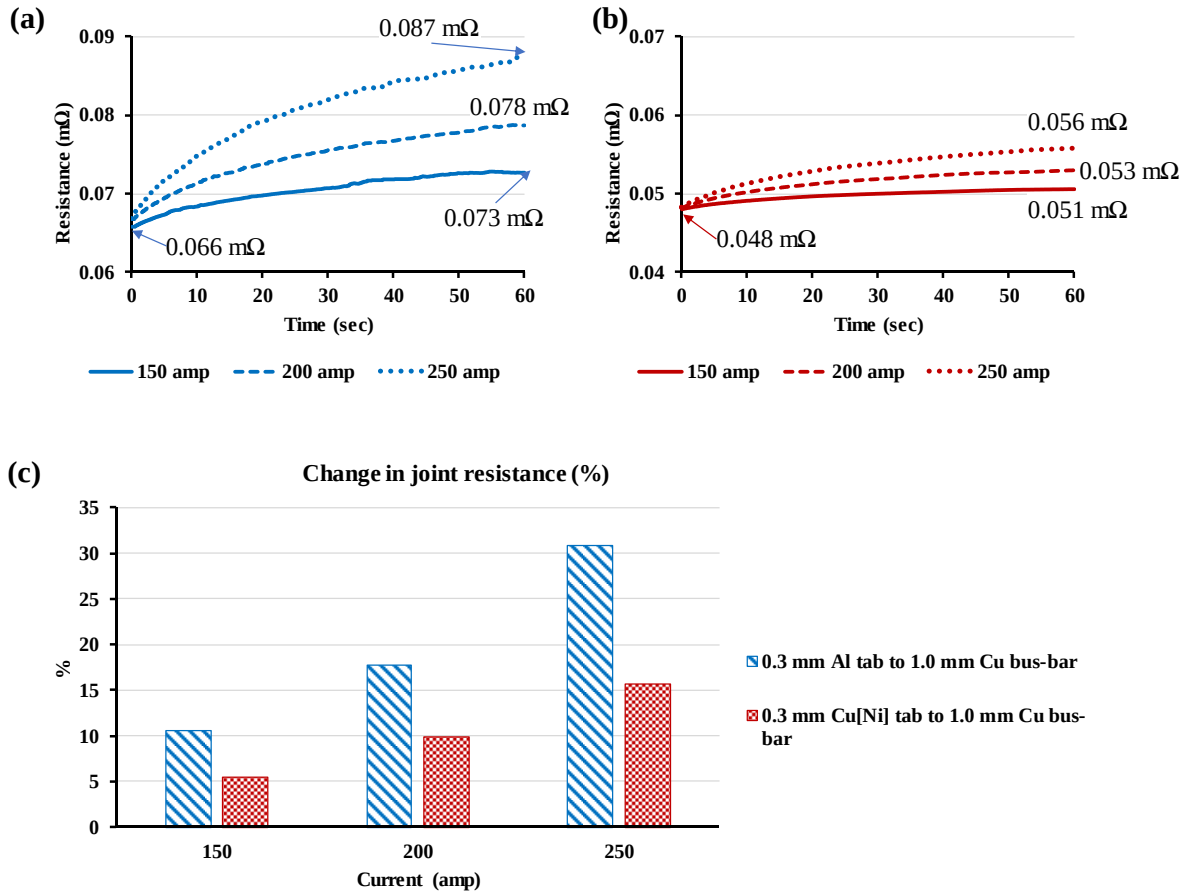

Fig. 4, the electrical resistance behaviours for two different joint configurations (i.e. Al/Cu[Ni] tabs to Cu bus-bar) are shown when the different amplitudes of current were passed through the joints for 60 sec. It can be observed that, as expected, the resistance is slowly increasing within the period of current application, higher the applied current higher rate of increase. When the current was passed through the welded joint, as a result of resistive heat loss, the generated heat increased the resistance of the joint, worked as a positive feedback loop. For 0.3 mm Al tab to 1 mm Cu bus-bar sample, the values of resistance at the beginning was around 0.066 mΩ irrespective of the applied current. At the end of 60 sec current flow, the resistance

increased close to 0.073 mΩ for 150 A current, 0.078 mΩ for 200 A and 0.087 mΩ for 250 A current, which are around 10.5 %, 17.7 % and 30.8 % resistance increase respectively. Similarly, for 0.3 mm Cu[Ni] tab to 1 mm Cu the values of resistance at the beginning was around 0.048 mΩ irrespective of the applied current. At the end of 60 sec current flow, the resistance increased close to 0.051 mΩ for 150 A current, 0.053 mΩ for 200 A and 0.056 mΩ for 250 A current, which are around 5.4 %, 9.8 % and 15.7 % resistance increase respectively. The joint resistance and the relative changes for 0.3 mm Cu[Ni] tab to 1 mm Cu bus-bar were comparatively lower than the corresponding values for 0.3 mm Al tab joints. The lower resistance for copper to copper case mainly due to the fact that the nickel coated copper is better conductor than aluminium and the issues of dissimilar metal joint is avoided. The lower resistance raise over 60 sec period mainly due to the fact that copper has faster heat dissipation properties than aluminium, and lower amount of heat was generated for copper when current start to flow, this will be discussed in-details in Section 5.2.

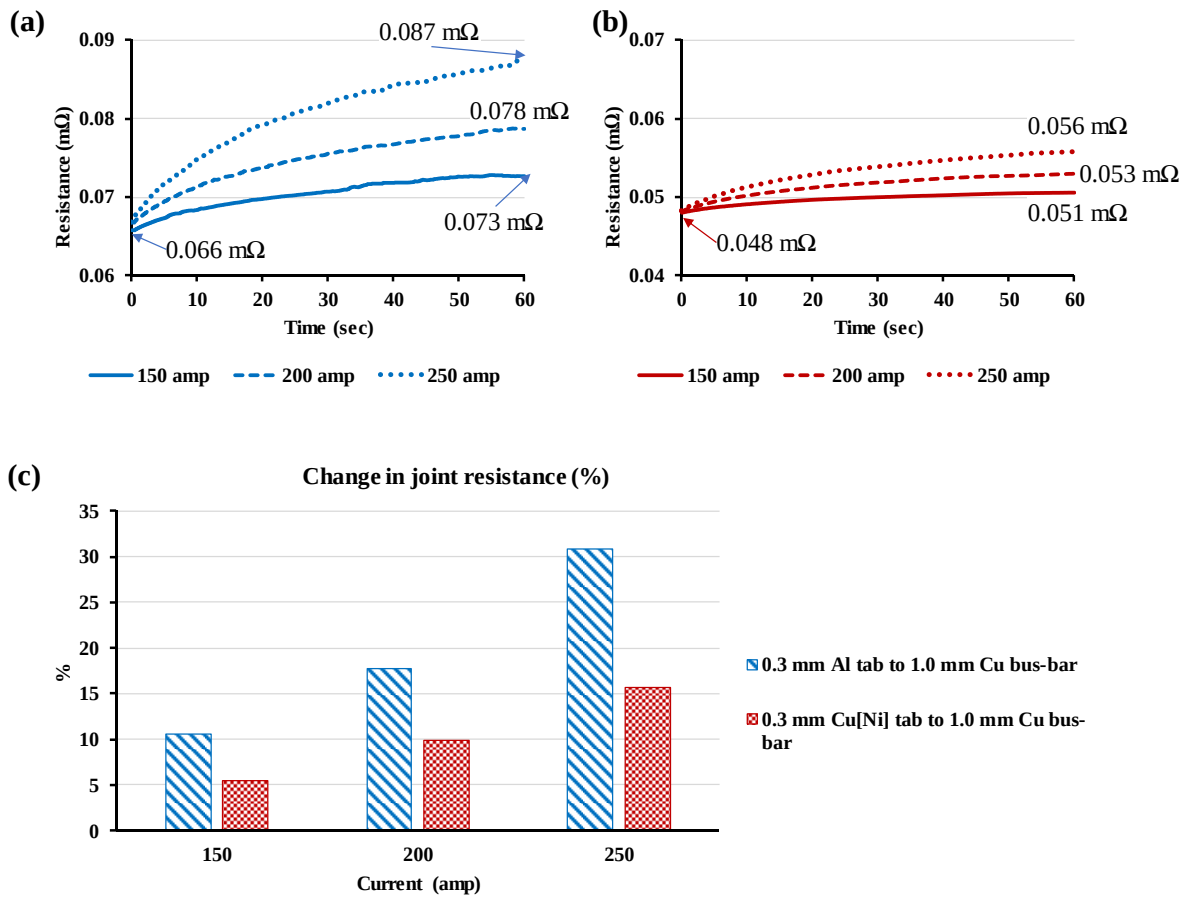

Fig. 4 Electrical resistance change behaviours for two joint configurations (a) 0.3 mm Al tab to 1 mm Cu bus-bar joint, (b) 0.3 mm Cu[Ni] tab to 1 mm Cu bus-bar joint and (c) the relative change of resistance when 150, 200 and 250 Amp current were employed.

5.2. Temperature distribution

As explained in Section 3.3, the temperatures of the joint along with tab and bus-bar materials increased due to the resistance and subsequent heat generation (I^2R_{weld}). The temperature profiles of the welded area due to different current amplitude are plotted in Fig. 5 for both joint configurations. Similar to the resistance figure, increase of temperature for 0.3 mm Al tab to 1 mm Cu bus-bar joint was comparatively higher than the 0.3 mm Cu[Ni] tab to 1 mm Cu bus-bar. For example, at 200 amp and 250 amp current values, the maximum temperature obtained from 0.3 mm Al tab to 1 mm Cu bus-bar joint were 53.26°C and 73.25°C, whereas slightly lower temperatures 39.44°C and 49.02°C were recorded for 0.3 mm Cu[Ni] tab to 1 mm Cu bus-bar joint, respectively. Fig. 5 (c) shows the thermal image of the joint area, captured during the test. The temperature distribution found to be homogeneous across the joint area. This temperature increase above 40° have a consequence on premature ageing of the battery [28]; however, beyond 70°C it poses safety risk as it exceeds the safe operating limit of most commercial Li-ion battery cell [29, 30].

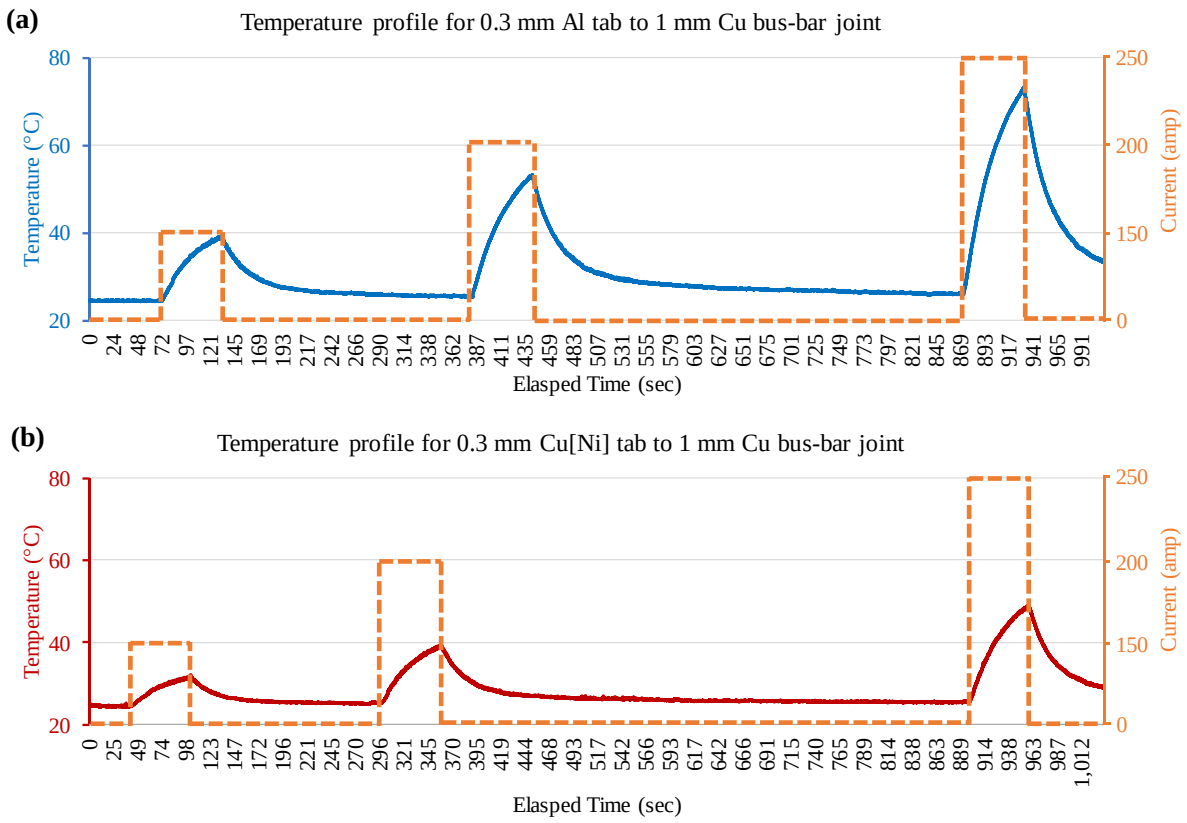

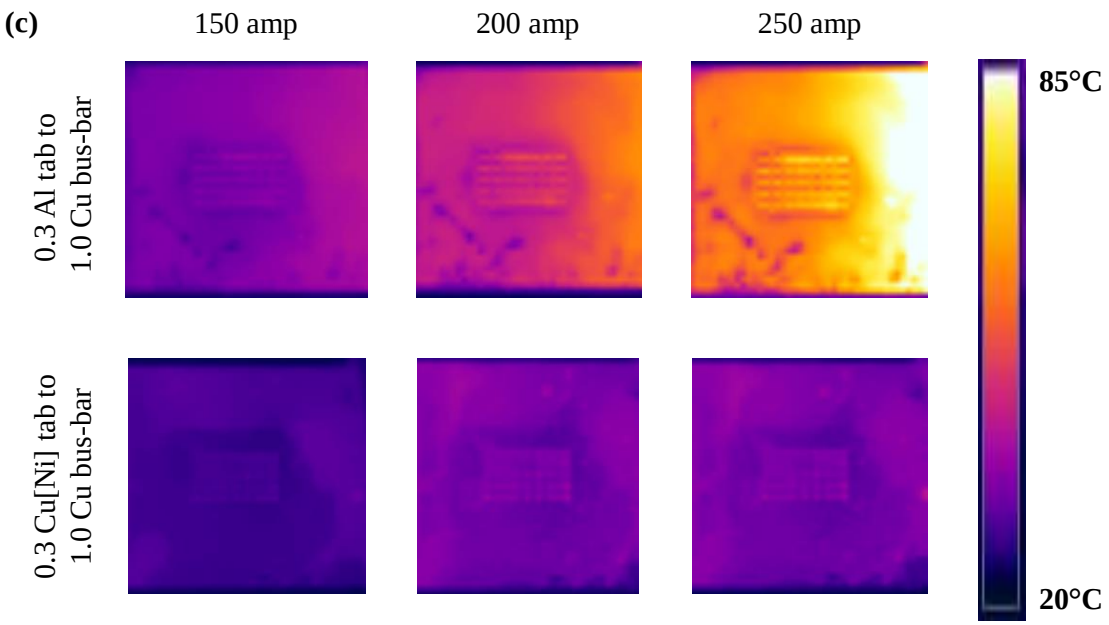

Fig. 5 Temperature profile as a result of current flow and corresponding resistance change (a) 0.3 mm Al tab to 1 mm Cu bus-bar joint, and (b) 0.3 mm Cu[Ni] tab to 1 mm Cu bus-bar joint, (c) IR thermal images from the test for different current values at maximum temperature.

In this experiment, the joint area was exposed to the environment, allowing maximum heat dissipation to the environment. However, in real battery the joint area is likely to be confined to a tight closed environment, indicating temperature could increase much higher than shown in Fig. 5. Although, commercial battery packs have active or passive thermal management system (TMS) [31], however, they are mainly designed focusing on cell surface cooling, rather than the bus-bar, therefore, temperature hotspots still could exist within the battery pack having a TMS.

Another alarming factor is, most of the temperature sensors within a battery pack are placed within the cell surface [31, 32]. For the same amount of current, temperature on the cell surface could be much lower than at the welded area. For example, in a recent work Hosseinzadeh *et al*. [33] applied a race cycle, dominated by 300 Amp discharge pulses, to a commercial cell having aluminium and copper tabs (similar to the ones used in this study), for 30 min. The cell temperature raise they observed was 43 °C from the ambient temperature of 25 °C. From the results presented in Fig. 5, the temperature raise at the welding area will be higher than 50 °C for copper tab and more than 75 °C for aluminium tab. This shows the importance of a low resistance welded area and the thermal management for the welding area, Hunt *et al*. [34]

already shown a lower battery ageing can be achieved when battery tab area is cooled rather than the cell surface.

As mentioned earlier, the temperature raise shown in Fig. 5 is strongly affected by the change of resistance while battery heats up and heat dissipation to the environment, this two factors can be accounted for employing numerical modelling techniques and temperature raise can be estimated for the conditions when heat dissipation is restricted as present within a battery pack, following section will focus on that.

5.3. Electrical and thermal modelling

To simulate the temperature raise, it is estimated that the samples were tested at an ambient temperature of 296.15 K. Ohmic heating is the only heat source (in the energy equation, eq. 2) and the natural convection acts on the surface to cool the geometry. Therefore, the temperature profile on the surface and weld region is a function of the applied current, electrical resistance, heat transfer coefficient and the surface area. Thermal conductivity of the material is also important through the flux continuity (in the equation, eq. 4) described in Section 4. The Ohmic resistance has contribution from the property of the material.

The experimental inputs for the 250A case are taken for parameterising the simulation in which the external convective heat transfer coefficient is carefully adjusted to match the measured temperature with the simulated temperature. A series of parametrisations studies are conducted by varying the convective heat transfer coefficient over the aluminium tab, copper bus bar and the weld joint. It has been observed that a heat transfer coefficient of 6 W/m^2K imposed over the surfaces result in 73.65°C over weld region. This heat transfer coefficient testifies that the geometry is kept in a natural convection environment where the expectation is within the range of 2~7 W/m^2K for a natural convection case. Due care is taken to keep the simulated results within ±2 °C of the experimental values. Fig. 6 shows the simulated steady state temperature distribution over three different regions of the weld joint while 250A current is applied across the ends. Fig. 6a shows the temperature distribution over the full geometry under steady state condition. The area near to the weld region experiences the highest thermal gradient $\left({}^{\Delta T}/_{\Delta x}\right)$ therefore highest thermal stress whereas the copper bus-bar is at constant temperature (Fig. 6c). The Ohmic heating in copper bus bar is less significant compared to aluminium tab.

Fig. 6b, shows high temperature on the aluminium bus bar, which is due to higher Ohmic heating because of higher resistance of the aluminium. The thermal gradients near the weld region indicates that the heat is conducted from the aluminium tab through the weld to the

copper bus bar. Therefore, the thermal stress could be significant near to the weld region and can be neglected for the regions away from weld. To validate this assumption, an energy balance table is presented in Table 3. Maximum heat is generated on the aluminium tab and minimum on the copper bus-bar. The volume average temperature in the weld region has contributions from the Ohmic heat as well as the heat conducted from aluminium tab to copper bus-bar.

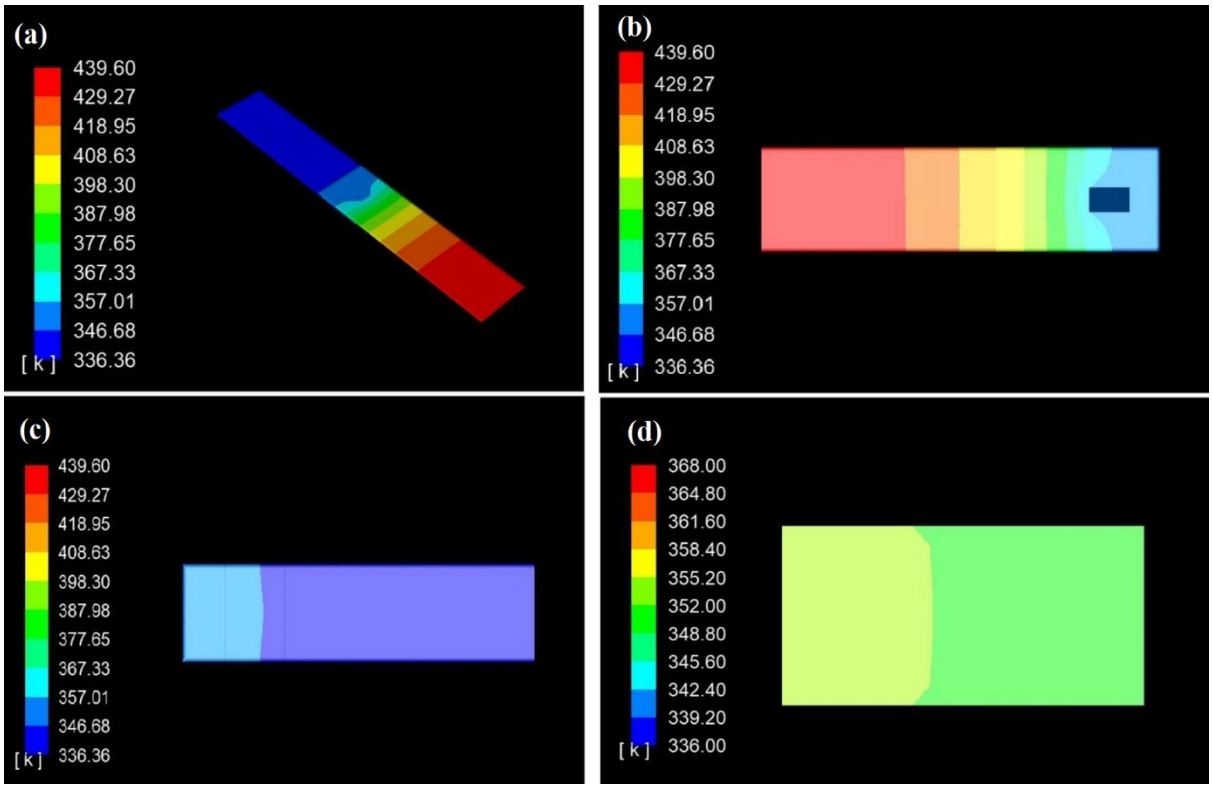

Fig. 6 Temperature distribution of 0.3mm Al tab to 1.0mm Cu bus-bar with 250A current flow a) Full isometric view of the simulated geometry b) 0.3 mm Aluminium tab c) 1.0mm Copper bus-bar d) weld region.

Table 3 An estimate of Joule heating in the weld geometry and the average temperature.

0.3mm Al tab to 1.0mm Cu bus bar						
Applied current	**250A**		**200A**		**150A**	
	Joule heating (W)	Volume average temperature	Joule heating (W)	Volume average temperature (K)	Joule heating (W)	Volume average temperature (K)
Aluminium tab	21.23	394.18	13.69	314.24	6.17	343.03
Weld region	0.56	343.87	0.3669	310.58	0.026	315.75

Copper bus-bar	0.059	334.29	0.0382	300.348	0.016	312.07

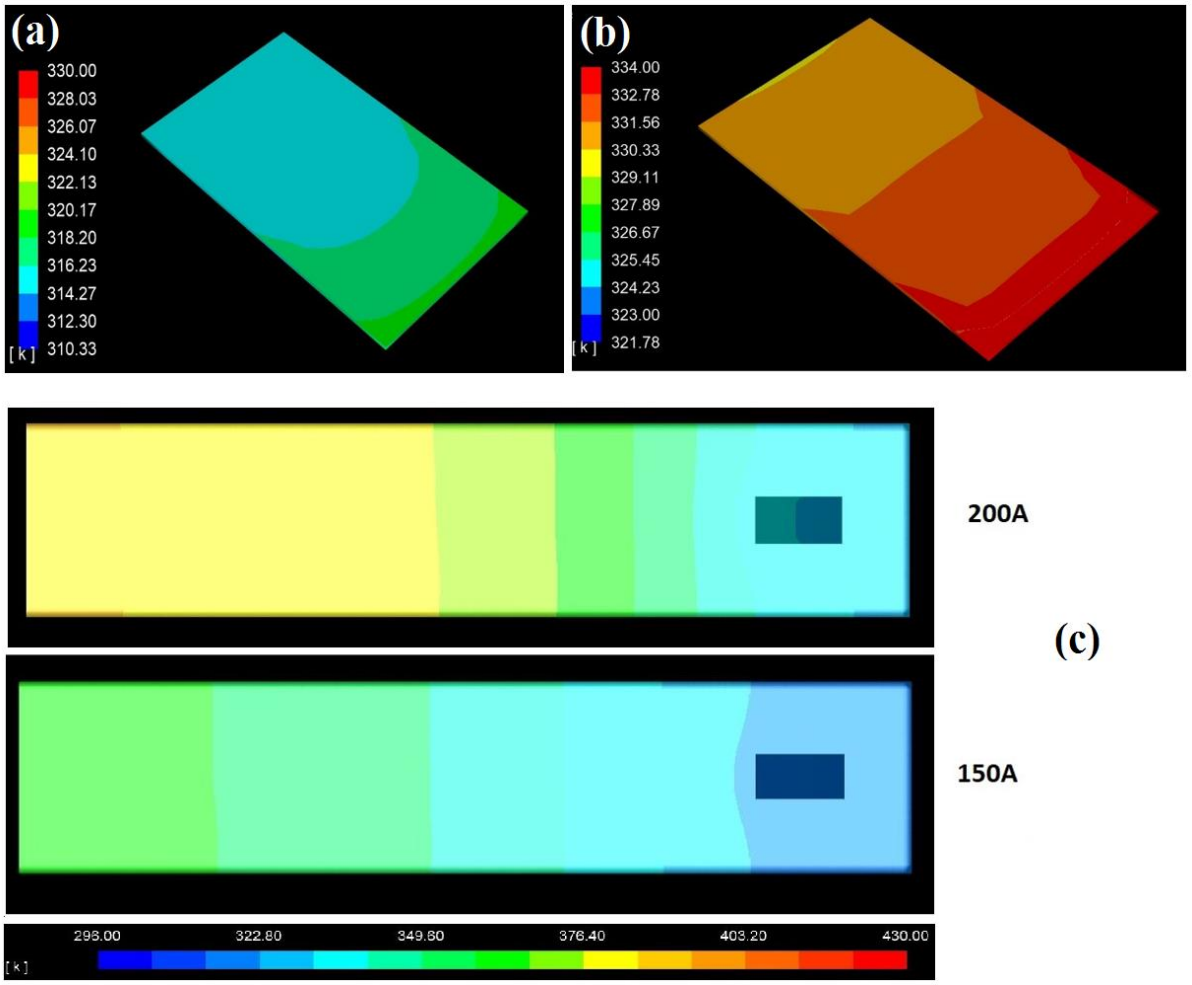

Fig. 7 Validation temperature profiles on the weld region a) with 150A current b) with 200A current. c) Temperature distribution of 0.3mm Al tab at 150A and 200A peak current.

Fig.7 shows the simulated temperature distribution over the weld region and aluminium tab for the validating cases of 150A and 200A in comparison with 250A case, which is taken for parametrising the model. Thermal diffusivity ($\alpha = k/\rho C_p$) of the weld geometry is the key to decide the initial rate of increase of temperature in the system. A geometry with higher thermal conductivity (k) will be favourable for equilibrating the temperature distribution within less time, whereas the geometry with a higher heat capacity (C_p) or density (ρ) tries to store more energy within, and can take longer time to reach steady state. Fig.7 shows the 150A case is showing contour of temperatures ranging from 37 °C to 43 °C within the weld region. This observation matches well with the measured temperature recorded 39.44°C. Similarly, 200A current shows a temperature contour ranging from 48 °C to 56 °C, which is within the

experimentally measured value of 53.26°C. In the above validation cases, the simulated temperature is within ±2 °C compared to the experimental measurements.

The steady state temperature profile on the geometry shows that the weld geometry must be placed in a forced convection environment or a natural convection environment to reduce temperature on the tab as well as weld regions. But the results for a confined space experiment (without heat transfer) is still unknown. To find the rate of temperature increase, following confined space transient simulation is conducted which shows the temperature on geometry kept in such an environment without heat transfer increases drastically. Fig. 8 shows temperature profile over the test setup kept in an insulated condition. The convective heat transfer coefficient is reduced to a minimum value, which will prevent any heat loss simulating an insulated condition. However, heat conduction in the geometry is still a predominant phenomenon. A time step of 0.1 second and 20 inner iterations per time step is chosen for stability. It has been observed that the energy equation and the potential source term is reaching the required convergence criteria 1×10^{-12} much before 20 iterations. Fig. 8a and Fig. 8b shows the temperature distribution over the test setup after 15 seconds of operation with 150A current and 200A current. There is a significant increase in temperature on aluminium tab, in zones away from the weld region. Temperature increase of 68.79 °C and 122.32°C can be observed over the ambient temperature (23 °C) within 15 seconds, emphasis the need for a proper cooling condition for high current battery operations. Fig 8c and Fig 8d shows the volume average temperature in different zones with 150A and 200A over a period of 60 seconds. The volume average temperature over the aluminium tab is reaching 150°C for 150A current and 200°C for 200A current. Both conditions have the possibility of reaching the melting temperature of aluminium resulting in severe structural damage. Moreover, the heat can propagate into the battery through conduction, which has significant impact on the kinetic properties of the chemicals used in battery leading to dissociation of battery chemicals thereby altering the chemical kinetic properties.

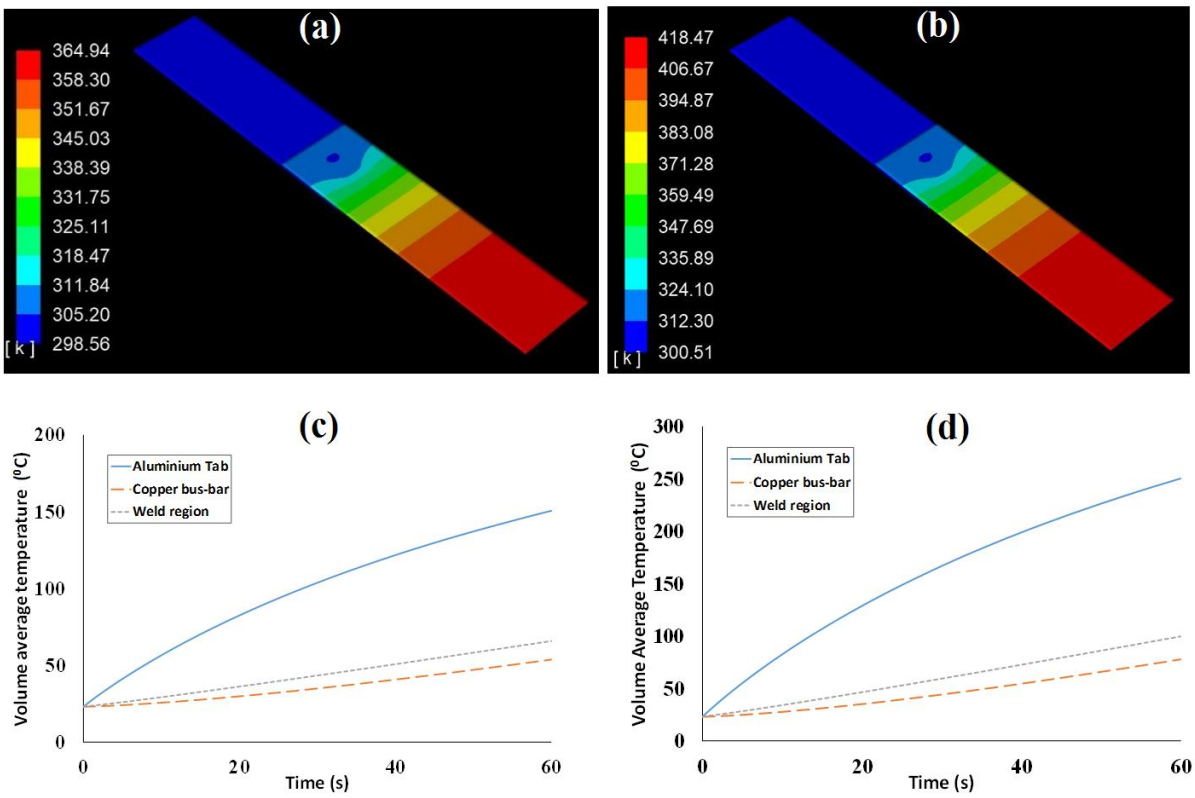

Fig. 8 Temperature distribution on the geometry after 15 seconds of operation with adiabatic condition a) 150A and b) 200A- Volume average temperature increase in each zone with adiabatic condition c) 150A and d) 200A

Temperature is identified as one of the critical stress factors affecting battery performance. Exposing battery to high temperature can accelerate ageing or solid electrolyte interface growth leading to premature cell failure. These results are giving an indication of employing proper cooling over the tab, bus bar geometry to minimise the damage associate with improper cooling.

6. Conclusions

In this article, for the first time, electrical and thermal behaviour of battery tabs to copper busbar joints were investigated. When current was passed through the joints the temperature increases, due to resistive heat loss at the joint. The temperature of aluminium tab to copper busbar joint was increasing to 53.26 °C and 73.25 °C from room temperature (23 °C) when a short current pulses of 200 A and 250 A were passed respectively. The respective values for copper tab to copper busbar were 39 °C and 49 °C. The difference of the temperature raise mainly originated from the difference in resistance of aluminium and copper and due to dissimilar metallic joint for aluminium to copper. The temperature raise led to increase of the resistance of the joint,

which within a minute can raise by 30.8 % for aluminium tab to copper bus-bar joint and 15.7 % for copper tab to copper bus-bar joint. This increase of resistance, increased the resistive heat loss, therefore, the further temperature raise, a positive feedback loop exist.

To estimate the temperature raise within confined space as in the battery pack, a numerical model was developed and parameterised. The model suggest, the temperature at the welded spot can raise close to 100 °C for copper to copper joints and higher than 200 °C for aluminium to copper joints. This high temperature raise may lead to premature ageing of battery, and subsequently, exceeds the safe operating limit of most commercial Li-ion battery cells.

In most of the commercial battery pack, the TMS are designed for cell surface cooling, rather than the tab to bus-bar joints, therefore, temperature hotspots still could exist within the battery pack having a TMS. This research suggest thermal management of battery cells within a pack might be better achieved through busbar and tab cooling. Furthermore, this article directs towards the future research attention needed for selection of tab and bus-bar materials and suitable joining techniques to produce low resistance joint.

Acknowledgement

This research is partially supported by the WMG Centre High Value Manufacturing (HVM) Catapult at WMG, The University of Warwick.

Reference

[1] Amending Regulation (EC) No 443/2009 to define the modalities for reaching the 2020 target to reduce CO2 emissions from new passenger cars, in: The European Parliament and The Council of the European Union (Ed.) Regulation (EU) No 333/2014, Official Journal of the European Union, 2014.
[2] National Research Council. 2010. Advancing the Science of Climate Change. Washington, DC: The National Academies Press.
[3] UK Government, Climate Change Act 2008, in: UK Government (Ed.), 2008.
[4] M.M. Thackeray, C. Wolverton, E.D. Isaacs, Electrical energy storage for transportation-approaching the limits of, and going beyond, lithium-ion batteries, Energy & Environmental Science, 5 (2012) 7854-7863.
[5] S. Manzetti, F. Mariasiu, Electric vehicle battery technologies: From present state to future systems, Renewable and Sustainable Energy Reviews, 51 (2015) 1004-1012.
[6] S.S. Lee, T.H. Kim, S.J. Hu, W.W. Cai, J.A. Abell, Joining Technologies for Automotive Lithium-Ion Battery Manufacturing: A Review, in: ASME 2010 International Manufacturing Science and Engineering Conference, Pennsylvania, USA, 2010, pp. 541-549.

[7] M.J. Brand, P.A. Schmidt, M.F. Zaeh, A. Jossen, Welding techniques for battery cells and resulting electrical contact resistances, Journal of Energy Storage, 1 (2015) 7-14.
[8] A. Das, D. Li, D. Williams, D. Greenwood, Joining Technologies for Automotive Battery Systems Manufacturing, World Electric Vehicle Journal, 9 (2018) 22.
[9] L. Lu, X. Han, J. Li, J. Hua, M. Ouyang, A review on the key issues for lithium-ion battery management in electric vehicles, Journal of Power Sources, 226 (2013) 272-288.
[10] N. Nitta, F. Wu, J.T. Lee, G. Yushin, Li-ion battery materials: present and future, Materials Today, 18 (2015) 252-264.
[11] D. Deng, Li-ion batteries: basics, progress, and challenges, Energy Science & Engineering, 3 (2015) 385-418.
[12] A. Das, D. Li, D. Williams, D. Greenwood, Weldability and shear strength feasibility study for automotive electric vehicle battery tab interconnects, Journal of the Brazilian Society of Mechanical Sciences and Engineering, 41 (2019) 54.
[13] A. Das, I. Masters, D. Williams, Process robustness and strength analysis of multi-layered dissimilar joints using ultrasonic metal welding, Int J Adv Manuf Technol, (2018).
[14] M. Shakil, N.H. Tariq, M. Ahmad, M.A. Choudhary, J.I. Akhter, S.S. Babu, Effect of ultrasonic welding parameters on microstructure and mechanical properties of dissimilar joints, Materials & Design, 55 (2014) 263-273.
[15] W. Cai, P.J. Blau, J. Qu, Friction coefficients of battery metals and the usage in ultrasonic welding simulations, in: 2013 World Electric Vehicle Symposium and Exhibition (EVS27), 2013, pp. 1-10.
[16] H. Li, H. Choi, C. Ma, J. Zhao, H. Jiang, W. Cai, J.A. Abell, X. Li, Transient Temperature and Heat Flux Measurement in Ultrasonic Joining of Battery Tabs Using Thin-Film Microsensors, Journal of Manufacturing Science and Engineering, 135 (2013) 051015-051015-051018.
[17] Z.L. Ni, F.X. Ye, Dissimilar Joining of Aluminum to Copper Using Ultrasonic Welding, Materials and Manufacturing Processes, 31 (2016) 2091-2100.
[18] S. Elangovan, S. Semeer, K. Prakasan, Temperature and stress distribution in ultrasonic metal welding—An FEA-based study, Journal of Materials Processing Technology, 209 (2009) 1143-1150.
[19] E. De Vries, Mechanics and mechanisms of ultrasonic metal welding, in, The Ohio State University, 2004.
[20] C. Zhang, L. Li, A Coupled Thermal-Mechanical Analysis of Ultrasonic Bonding Mechanism, Metallurgical and Materials Transactions B, 40 (2009) 196-207.
[21] A. Siddiq, E. Ghassemieh, Thermomechanical analyses of ultrasonic welding process using thermal and acoustic softening effects, Mechanics of Materials, 40 (2008) 982-1000.
[22] T.H. Kim, J. Yum, S.J. Hu, J.P. Spicer, J.A. Abell, Process robustness of single lap ultrasonic welding of thin, dissimilar materials, CIRP Annals - Manufacturing Technology, 60 (2011) 17-20.
[23] S. Shawn Lee, T. Hyung Kim, S. Jack Hu, W.W. Cai, J.A. Abell, J. Li, Characterization of Joint Quality in Ultrasonic Welding of Battery Tabs, Journal of Manufacturing Science and Engineering, 135 (2013) 021004-021013.
[24] B. Kang, W. Cai, C.-A. Tan, Dynamic Stress Analysis of Battery Tabs Under Ultrasonic Welding, Journal of Manufacturing Science and Engineering, 136 (2014) 041011.
[25] S. Choi, T. Fuhlbrigge, S. Nidamarthi, Vibration analysis in robotic ultrasonic welding for battery assembly, in: IEEE International Conference on Automation Science and Engineering (CASE), 2012, pp. 550-554.
[26] C. Yuan, Y. Deng, T. Li, F. Yang, Manufacturing energy analysis of lithium ion battery pack for electric vehicles, CIRP Annals, 66 (2017) 53-56.

[27] T.R. Ashwin, G.S.V.L. Narasimham, S. Jacob, Oscillatory flow and temperature fields in an open tube with temperature difference across the ends, International Journal of Heat and Mass Transfer, 54 (2011) 3357-3368.
[28] F. Leng, C.M. Tan, M. Pecht, Effect of Temperature on the Aging rate of Li Ion Battery Operating above Room Temperature, Scientific reports, 5 (2015) 12967-12967.
[29] A.M. Aris, B. Shabani, An Experimental Study of a Lithium Ion Cell Operation at Low Temperature Conditions, Energy Procedia, 110 (2017) 128-135.
[30] T.M. Bandhauer, S. Garimella, T.F. Fuller, A Critical Review of Thermal Issues in Lithium-Ion Batteries, 158 (2011) R1-R25.
[31] N. Javani, I. Dincer, G.F. Naterer, G.L. Rohrauer, Modeling of passive thermal management for electric vehicle battery packs with PCM between cells, Applied Thermal Engineering, 73 (2014) 307-316.
[32] S. Arora, A. Kapoor, W. Shen, A novel thermal management system for improving discharge/charge performance of Li-ion battery packs under abuse, Journal of Power Sources, 378 (2018) 759-775.
[33] E. Hosseinzadeh, R. Genieser, D. Worwood, A. Barai, J. Marco, P. Jennings, A systematic approach for electrochemical-thermal modelling of a large format lithium-ion battery for electric vehicle application, Journal of Power Sources, 382 (2018) 77-94.
[34] I.A. Hunt, Y. Zhao, Y. Patel, J. Offer, Surface Cooling Causes Accelerated Degradation Compared to Tab Cooling for Lithium-Ion Pouch Cells, Journal of The Electrochemical Society, 163 (2016) A1846-A1852.